Journal of Applied Fluid Mechanics, Vol. 16, No. 3, pp. 561-573, 2023.
Available online at www.jafmonline.net, ISSN 1735-3572, EISSN 1735-3645.
https://doi.org/10.47176/jafm.16.03.1343

Numerical Study of Microstructures and Roughness Design Effects on Surface Hydrophilicity through the Lattice Boltzmann Method

X. Y. Zhang[1], G. Q. Sun[1], C. Li[2, 3, 4], Y. M. Ding[2, 3, 4 †]and X. B. Luo[1]

[1] *School of Energy and Power Engineering, Huazhong University of Science and Technology, Wuhan 430074, China*
[2] *Department of Stomatology, Union Hospital, Tongji Medical College, Huazhong University of Science and Technology, Wuhan 430022, China*
[3] *School of Stomatology, Tongji Medical College, Huazhong University of Science and Technology, Wuhan 430030, China*
[4] *Hubei Province Key Laboratory of Oral and Maxillofacial Development and Regeneration, Wuhan 430022, China*

†*Corresponding Author Email: yumeiding@hust.edu.cn*

(Received May 27, 2022; accepted November 11, 2022)

ABSTRACT

Hydrophilicity is one of the most vital characteristics of titanium (Ti) implants. Surface structure design is a powerful and efficient strategy for improving the intrinsic hydrophilic ability of Ti implants. Existing research has focused on experimental exploration, and hence, a reliable numerical model is needed for surface structure design and corresponding hydrophilicity prediction. To address this challenge, we proposed a numerical model to analyze the droplet dynamics on Ti surfaces with specific microstructures designed through the lattice Boltzmann method (LBM). In this work, a Shan-Chen (SC) model was applied in the simulations. We simulated droplets spreading on smooth and micropillar surfaces with various wettability and provided a comprehensive discussion of the edge locations, contact line, droplet height, contact area, surface free energy, and forces to reveal more details and mechanisms. To better tune and control the surface hydrophilicity, we investigated the effects of micropillar geometric sizes (pillar width a, height h, and pitch b) on hydrophilicity via single factor analysis and the response surface method (RSM). The results show that the hydrophilicity initially increases and then decreases with an increasing a, increases with an increasing h, and decreases with an increasing d. In addition, the interaction effects of a-d and h-d are significant. The optimization validation of the RSM also demonstrates the accuracy of our lattice Boltzmann (LB) model with an error of 0.687%. Here, we defined a dimensionless parameter ξ to integrate the geometric parameters and denote the surface roughness. The hydrophilicity of Ti surfaces improves with an increasing surface roughness. In addition, the effect of the microstructure geometry shape was investigated under the same value of surface roughness. Surfaces with micropillars show the best hydrophilicity. Moreover, this study is expected to provide an accurate and reliable LB model for predicting and enhancing the intrinsic hydrophilicity of Ti surfaces via specific microstructure and roughness designs.

Keywords: Ti implant; LBM; Microstructure; Surface roughness; RSM; Hydrophilicity enhancement.

1. INTRODUCTION

Titanium (Ti) has been widely used in the biomedical field of orthopedic and dental implants due to its excellent properties, such as biocompatibility, chemical stability and corrosion resistance, light weight, and machinability (Mosas *et al.* 2022). However, the biological inertness of Ti inhibits implant contacts and combinations with osteoblasts and proteins, which will cause poor osseointegration and implantation failure (Dong *et al.* 2021). Enhancing the hydrophilicity of the implant surface is an effective and common method to solve this problem, thus promoting osseointegration and therapeutic effects (Liddell *et al.* 2020).

Many surface modification methods have been proposed to enhance the hydrophilicity of Ti surfaces; these methods are mainly divided into additional coating methods and surface structure design. The additional coating methods increase the surface hydrophilicity by taking advantage of the hydrophilic biomaterials. Biomaterials used for implant coatings are broadly classified into ceramics (Díaz-Cuenca *et al.* 2022; Li *et al.* 2022), polymers (Tao *et al.* 2020; Tallet *et al.* 2021), and metallic systems (Pham *et al.* 2022; Yan *et al.* 2022). However, the problems of cytotoxicity, shedding of coatings, and a lack of mechanical properties still exist. Compared with the additional coating methods, surface structure design is a reliable and efficient strategy for improving the intrinsic hydrophilic ability of Ti surfaces (Yang and Huang 2021).

The surface structure design enhances the hydrophilicity by generating micro/nanoscale structures on Ti surfaces. The effectiveness of several surface treatment techniques, such as sand-blasting large grit acid-etching (SLA) (Park *et al.* 2022), alkali-heat-treatment (Wang *et al.* 2021), and anodic oxidation (Zhang *et al.* 2021), have been widely investigated. To achieve a possible optimization on the industrial level, it is important to conduct feasibility studies on the complex designs of structure sizes and shapes. Abhijith *et al.* (2021) fabricated micro-grooves with embedded nanoscale ripples on Ti surfaces via laser surface texturing (LST) and verified the enhancement of surface hydrophilicity and osseointegration. He *et al.* (2022) proposed a method that controls the hydrophilicity of Ti surfaces with either micro-protrusions or micro-grooves. The effect of the femtosecond laser process parameters on the shape of the microstructure was investigated. Existing research has focused on experimentally exploring the different hydrophilicities caused by various microstructures.

Due to limitations in the experiments, the specific mechanism and feasibility of complex structure design remain unclear. To address this challenge, it is necessary to establish a helpful numerical model. The lattice Boltzmann method (LBM) is a computational fluid dynamics method. Based on mesoscopic kinetics, the LBM is flexible and efficient to simulate multiphase flow (Du *et al.* 2017; Ezzatneshan 2019). Surface wettability is an important property (Davar *et al.* 2021), and the LBM is a commonly used and attractive method for analyzing droplet dynamics on solid surfaces (Zhang *et al.* 2018; Fei *et al.* 2022). Research on the effect of the surface micro/nanostructure has mainly focused on the hydrophobic surface (Mohammadrezaei *et al.* 2022) and the wettability transform (Yin *et al.* 2021). In view of the status quo, it is necessary to establish an accurate lattice Boltzmann (LB) model for analyzing the effects of microstructures and surface roughness on the hydrophilicity of Ti surfaces.

In this study, the LBM is utilized as a tool for modeling droplet dynamics on micro-structured Ti surfaces with various geometric sizes and shapes. First, we simulated droplet dynamics on smooth and micropillar surfaces with various wettability. The motions of the droplets were compared and discussed in terms of the edge locations, contact line, droplet height, contact area, and surface free energy. The forces were analyzed as well to obtain more knowledge about the mechanisms. Afterward, we discussed the effects of the micropillar geometric sizes on the surface hydrophilicity via a single factor analysis and the response surface method (RSM).

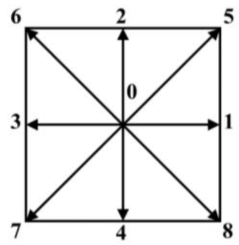

Fig. 1. Schematic of the discrete velocities in the D2Q9 model.

Here, the RSM was conducted to analyze the interaction of different geometric parameters and provide an optimal solution. Finally, a dimensionless parameter ξ was defined to integrate the geometric parameters and denote the surface roughness. The effect of the parameter ξ on the hydrophilicity of Ti surfaces was discussed. In addition, the effect of the microstructure geometric shapes was investigated under the same value of surface roughness.

2. LATTICE BOLTZMANN MODEL

There have been several LB model types, such as the color-fluid model (Wang *et al.* 2018), Shan-Chen model (Ezzatneshan and Goharimehr 2021), and free energy model (Sun *et al.* 2021). In this study, a Shan-Chen (SC) multi-component multi-phase model was applied for establishing the LB model (Ezzatneshan and Vaseghnia 2019; Panda *et al.* 2020). The SC model has been utilized extensively in the field of droplet wetting, and is computationally efficient for the calculation of the fluid–fluid cohesion and fluid–solid adhesion forces.

Figure 1 demonstrates the discrete velocities in the D2Q9 model (Lin *et al.* 2022). There are 9 discrete velocities for each site (lx, ly) represented by e_i:

$$e_i = \begin{cases} (0,0) & i = 0 \\ (\pm c,0),(0,\pm c) & i = 1 \sim 4 \\ (\pm c,\pm c) & i = 5 \sim 8 \end{cases} \tag{1}$$

For the SC model, the particle distribution function is described by:

$$f_{\sigma i}(x+e_i dt, t+dt) - f_{\sigma i}(x,t) = -\frac{1}{\tau}[f_{\sigma i}(x,t) - f_{\sigma i}^{eq}(x,t)] \tag{2}$$

where $f_{\sigma i}(x,t)$ is the particle distribution function at site x and time step t. Here, σ is the component, and i is the velocity direction. In addition, τ_σ indicates the relaxation time with a value of 1.0, and e_i is the discrete velocity. $f_{\sigma i}^{eq}(x,t)$ denotes the equilibrium distribution function given as:

$$f_{\sigma i}^{eq} = \omega_i \rho[1 + \frac{\mathbf{e}_i \cdot \mathbf{u}}{c_s^2} + \frac{(\mathbf{e}_i \cdot \mathbf{u})^2}{2c_s^4} - \frac{\mathbf{u}^2}{2c_s^2}] \tag{3}$$

In Eq. (3), c_s represents the lattice speed of sound. In addition, ω_i denotes the weight coefficient of the D2Q9 model. The values are listed below.

$$\omega_i = \begin{cases} 4/9, & i = 0 \\ 1/9, & i = 1 \sim 4 \\ 1/36, & i = 5 \sim 8 \end{cases} \tag{4}$$

For the component σ, the density is obtained according to:

$$\rho_\sigma(x,t) = \sum_i f_{\sigma i}^{eq} \tag{5}$$

The macroscopic velocity is calculated under the conditions of mass conservation and momentum conservation:

$$\mathbf{u} = \mathbf{u}' + \frac{\tau_\sigma F_\sigma}{\rho_\sigma} \tag{6}$$

where $\mathbf{u}'$ is a common velocity for each component calculated via:

$$\mathbf{u}' = \sum_\sigma \left(\sum_i \frac{f_{\sigma i} e_i}{\tau_\sigma}\right) / \sum_\sigma \frac{\rho_\sigma}{\tau_\sigma} \tag{7}$$

In Eq. (6), F_σ represents the force that acts upon the component σ. Moreover, F_σ consists of the fluid–fluid cohesion force F_c and solid–fluid adhesion force $F_{ads,\sigma}$, and is given by:

$$\boldsymbol{F}_\sigma = \boldsymbol{F}_{c,\sigma} + \boldsymbol{F}_{ads,\sigma} \tag{8}$$

$F_{c,\sigma}$ represents the cohesion force that acts upon the component σ defined as:

$$\boldsymbol{F}_{c,\sigma} = -G_c \rho_\sigma(x,t) \sum_i \omega_i \rho_{\bar{\sigma}}(x + \mathbf{e}_i \Delta t, t)\mathbf{e}_i \tag{9}$$

where σ and $\bar{\sigma}$ represent two kinds of components. In Eq. (9), G_c determines the fluid–fluid interfacial tension and thus controls the strength of $F_{c,\sigma}$. An overly large G_c will cause the phases to be immiscible. However, a G_c that is overly small will result in a mixture of both phases. The model is more stable when the following inequality holds (Huang *et al.* 2007):

$$1.6 < G_c\left(\rho_\sigma + \rho_{\bar{\sigma}}\right) < 2.0 \tag{10}$$

Here, we choose 1.8 as the value of the expression.

$F_{ads,\sigma}$ represents the adhesion force that exists in the solid–fluid interface described as:

$$\boldsymbol{F}_{ads,\sigma}(x) = -G_{ads,\sigma} \rho_\sigma(x,t) \sum_i \omega_i s(x + \mathbf{e}_i \Delta t)\mathbf{e}_i \tag{11}$$

In Eq. (11), a flag function $s(x + \mathbf{e}_i \Delta t)$ is defined to activate or deactivate $F_{ads,\sigma}$. The value of the function is either 1 or 0, indicating either a solid or a fluid site. $G_{ads,\sigma}$ is a parameter that reflects the solid–fluid interaction strength. In addition, the difference between $G_{ads,\sigma}$ determines the contact angle.

Based on Young's equation, a comparatively precise measurement of the contact angle is available via (Huang *et al.* 2007):

$$\cos\theta_e = \frac{G_{ads,2} - G_{ads,1}}{G_c(\rho_1 - \rho_2)/2} \tag{12}$$

where ρ_1 and ρ_2 denote the main density and associated dissolved density. The LB model is more stable if the adhesion parameters of the two components are in opposition, i.e., $G_{ads,1} = -G_{ads,2}$. Hence, the wettability of a solid surface is partly determined by the parameter $G_{ads,2}$.

In the calculation region, a spherical droplet with a radius of 25 was fixed at the top of microscale pillars. The initial densities were set to ρ_{liquid}=2.00 and ρ_{air}=0.06, and the cohesion parameter G_c equaled 0.87 according to Eq. (10).

For the simulations, the periodic boundary conditions were applied; thus, if the fluid left the calculation region from one side at a given time step, it then entered the calculation region from the opposite side at the next time step. In addition, the "bounce-back" was utilized at the solid wall to ensure that the solid nodes could not be penetrated by the liquid. The 2D micropillar structure was investigated, as shown in Fig. 2, where *a*, *h*, and *d* represent the pillar width, height, and pitch, respectively.

To establish a relationship between the dimensionless simulated results and the actual physical quantities, the length scale L_0, time scale T_0, and mass scale M_0 are needed. After multiplication by $[L_0]^{n_1}[T_0]^{n_2}[M_0]^{n_3}$, the simulated result will be converted to an actual physical quantity. In the simulations, L_0=1×10^{-6} *m*, T_0=1.866×10^{-7} *s*, and M_0=4.985×10^{-16} *kg* were used.

3. Results and Discussion

3.1 Study of the Grid Independence and Validation of the Contact Angle

3.1.1 Study of the Grid Independence

A study on the grid independence was conducted to discuss the effect of the grid size on the simulation. Here, the interaction strength $G_{ads,2}$ was set to 0.3,

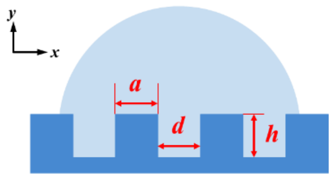

Fig. 2. Model of a droplet on the micropillar surface showing the pillar width *a*, height *h*, and pitch *d*.

indicating a static contact angle θ_e of 44° on a smooth Ti surface.

We simulated the static contact angle of droplets on the smooth surface and micropillar surface with different grid sizes. When changing the grid size, the initial radius of the water droplet and the geometric sizes of the micropillar were adjusted with equal proportions. Figure 3 shows the stable result of the contact angle and the corresponding time step with different grid sizes. The results suggest that the simulation result is accurate with less calculation time when selecting the calculation region with a 200×200 grid size. Therefore, the calculation region with a 200×200 grid size was used in the subsequent LBM simulations.

3.1.2 Validation of the Contact Angle

To verify the model, we simulated the static contact angle of droplets on smooth surfaces with different wettability. We also investigated the static contact angle of droplets on micropillar surfaces (a=5 μm, h=5 μm, and d=5 μm) to discuss the changes in wettability due to the addition of the surface micropillar.

In the numerical simulations, the initial densities were set to ρ_{liquid}=2.00 and ρ_{air}=0.06, and the cohesion parameter G_c equaled 0.87. Therefore, according to Eq. (12), we can adjust the wettability to control the static contact angle by changing the solid–fluid interaction force. Figure 4 displays the static contact angle (θ_e) as a function of the interaction strength ($G_{ads,2}$) on the smooth surface and micro-structured surface (a=5 μm, h=5 μm, and d=5 μm) when $G_{ads,1} = -G_{ads,2}$.

Regarding the smooth surface, the static contact angle decreases linearly with an increasing interaction strength. The formula value obtained from Eq. (12) is

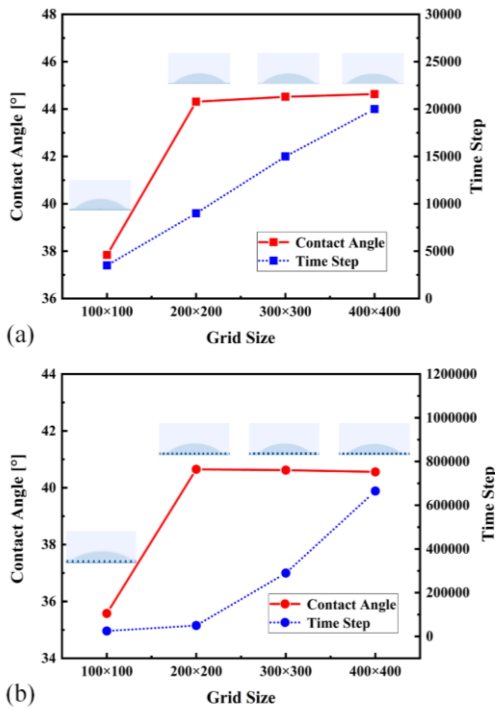

Fig. 3. Grid independence results on (a) the smooth surface and (b) the micropillar surface (*a*=5 *μm*, *h*=5 *μm*, and *d*=5 *μm*).

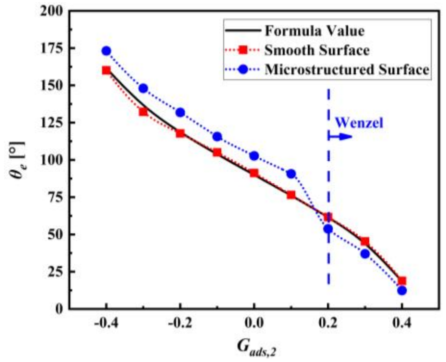

Fig. 4. Static contact angle (θ_e) as a function of the interaction strength ($G_{ads,2}$) on the smooth surface and micro-structured surface (*a*=5 *μm*, *h*=5 *μm*, and *d*=5 *μm*).

also shown in Fig. 4 to reflect the deviation. The simulation result of the smooth surface agrees well with the formula result over most of the range. Regarding the micropillar surface (a=5 μm, h=5 μm, and d=5 μm), the static contact angle decreases with an increasing interaction strength; this decrease is not linear and is different from that on the smooth surface. When $G_{ads,2}$ is less than 0.1, air exists between the droplet and micropillars, which is classified as the Cassie or partly Cassie state. In the Cassie state, the wettability property satisfies the following Cassie-Baxter equation (Cassie and Baxter 1944):

$$\cos\theta_c = f_s(1+\cos\theta_e)-1 \tag{13}$$

where f_s denotes the fraction of the solid–liquid interface of the droplets. For the same $G_{ads,2}$, the solid–liquid contact region of the micropillar surface is less than that of the smooth surface, leading to a smaller adhesion force and a larger contact angle. Therefore, the micropillar used in our simulations can enhance the hydrophobicity when $G_{ads,2}$ is less than 0.1. However, when $G_{ads,2}$ is more than 0.2, there is no air between the droplet and micropillars, which is classified as the Wenzel state. In the Wenzel state, the wettability property satisfies the following Wenzel equation (Wenzel 1936):

$$\cos\theta_w = r_f \cos\theta_e \tag{14}$$

where r_f represents the ratio of the real solid–liquid contact region to the projective region ($r_f \geq 1$). For the same $G_{ads,2}$, the solid–liquid contact region of the micropillar surface is greater than that of the smooth surface, which results in a larger adhesion force and a lower contact angle. Hence, the micropillar used in our simulations can enhance the hydrophilicity when $G_{ads,2}$ is more than 0.2.

3.2 Comparison of the Droplet Dynamics On Smooth and Micropillar Surfaces

To obtain more details and more information about the mechanisms, droplet dynamics on the smooth and micropillar surfaces (a=5 μm, h=5 μm, and d=5 μm) were simulated. Here, the interaction strength $G_{ads,2}$ was set to 0.3, indicating a static contact angle θ_e of 44° on a smooth Ti surface.

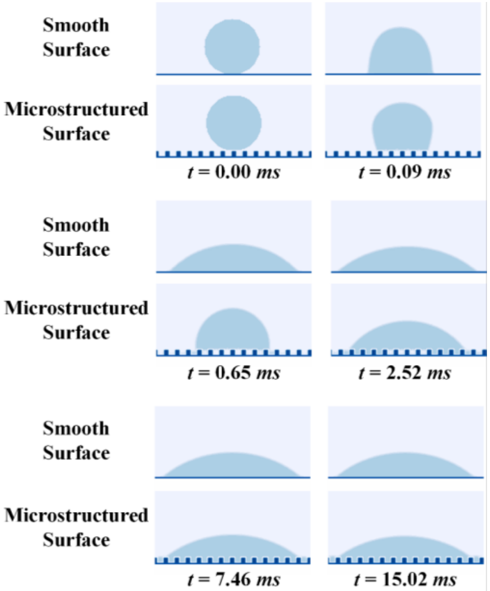

Fig. 5. Spreading of droplets on the smooth surface and micropillar surface (*a*=5 *μm*, *h*=5 *μm*, and *d*=5 *μm*).

Figure 5 shows the dynamic evolution of droplets on the smooth surface and micropillar surface. The droplet spreads faster on the smooth surface than on the micropillar surface. For the smooth surface, the droplet quickly spreads out into a flat shape before 0.65 *ms*. Afterward, there is no significant change in the droplet shape. For the micropillar surface, the droplet spreads more slowly. At the onset of the movement, there is no liquid in the spaces between the micropillars. As the droplet spreads, the liquid gradually falls into the spaces from the periphery. Finally, there is no air between the droplet and micropillars.

To quantitatively investigate the evolution of droplet movements, the locations of the droplet left edge and droplet right edge as well as the length of the contact line are plotted over time in Fig. 6. This shows that the droplet movement quickly becomes stable in Fig. 6(a). However, the spreading process is obviously slower in Fig. 6(b). In addition, due to the existence of micropillars, the curves in Fig. 6(b) are stepped shapes compared with the smooth curves in Fig. 6(a). Therefore, the surface micropillar used in our simulations stretches and impedes the spreading process.

As observed from Figs. 7(a) and 7(b), the evolution of the droplet height and solid–liquid contact area over time also demonstrates the stretching and hindering effect of the micropillar on the dynamic spreading process. In addition, compared with the smooth surface, the final droplet height on the micropillar surface is smaller, while the contact region is bigger. The differences indicate the preferable hydrophilicity of the micropillar surface.

Surface free energy calculation was conducted as well to examine the hydrophilicity, as shown in Fig. 7(c). According to the work of Wang *et al.* (2019), the surface free energy per unit area of a droplet reflects the interfacial tension. Hence, the surface free energy reflects the wettability of a solid surface to a certain extent. Here, we conduct a normalization of the surface free energy. The surface free energy at the beginning of droplet spreading is calculated by:

$$SE_0 = A_{la0}\gamma^{la} + A_{as0}\gamma^{as} \tag{15}$$

where A_{la0} and A_{as0} are the initial areas of the liquid–air and air–solid interfaces, respectively. The surface free energy of the droplet during the spreading movement is written as:

$$SE_1 = A_{la}\gamma^{la} + (A_{as} - A_{sl})\gamma^{as} + A_{sl}\gamma^{sl} \tag{16}$$

where A_{la}, A_{as}, and A_{sl} represent the corresponding areas of the liquid–air, air–solid, and solid–liquid interfaces, respectively. In addition, γ^{la}, γ^{as}, and γ^{sl} denote the surface tensions of the liquid–air, air–solid, and solid–liquid interfaces, respectively. The changed value of the surface free energy until the current time step is calculated by $\Delta SE = SE_1 - SE_0$:

$$\Delta SE = (A_{la} - A_{la0})\gamma^{la} + A_{sl}(\gamma^{sl} - \gamma^{as}) \tag{17}$$

Then, we divide ΔSE by γ^{la} to obtain the normalized surface free energy:

$$\frac{\Delta SE}{\gamma^{la}} = (A_{la} - A_{la0}) + \frac{A_{sl}(\gamma^{sl} - \gamma^{as})}{\gamma^{la}} \tag{18}$$

Young's equation describes the relationship between γ^{la}, γ^{as}, γ^{sl} and θ_e:

$$\gamma^{sl} - \gamma^{as} = -\gamma^{la}\cos\theta_e \tag{19}$$

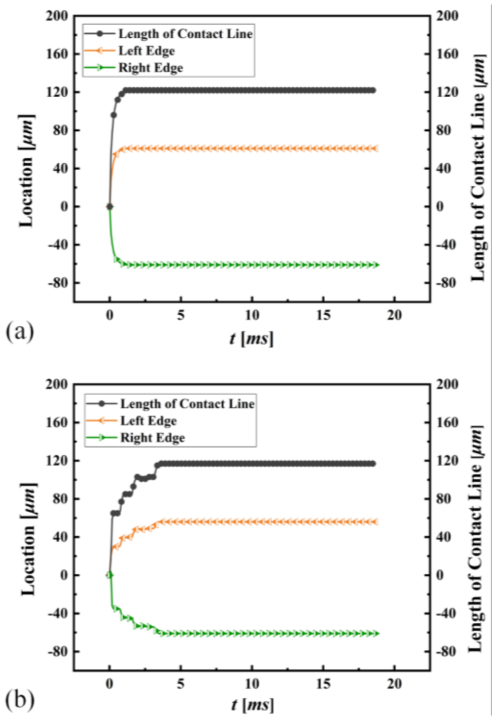

Fig. 6. Locations of the left and right edges as well as the length of the contact line over time on the (a) smooth surface and (b) micropillar surface (*a*=5 *μm*, *h*=5 *μm*, and *d*=5 *μm*).

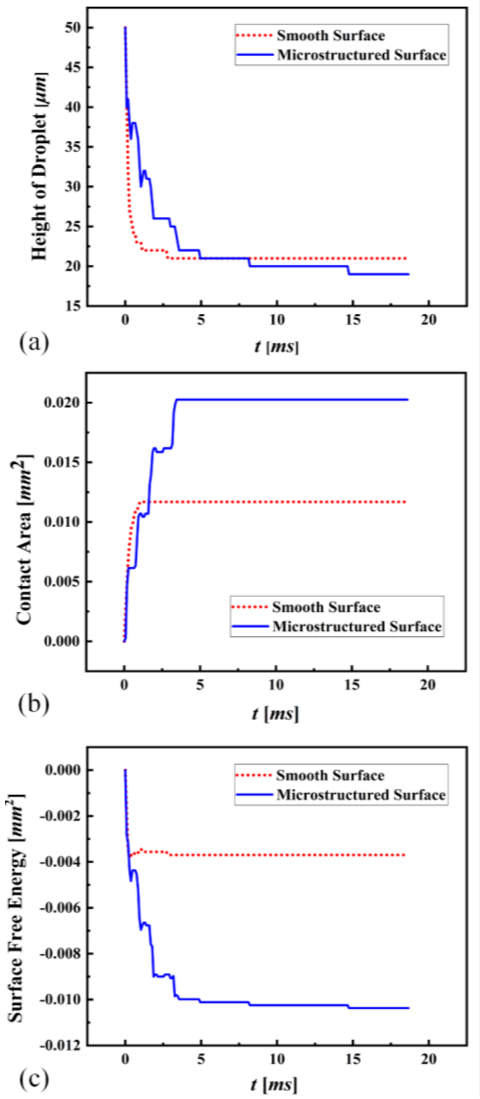

Fig. 7. Evolution of the (a) droplet height, (b) contact area, and (c) surface free energy over time.

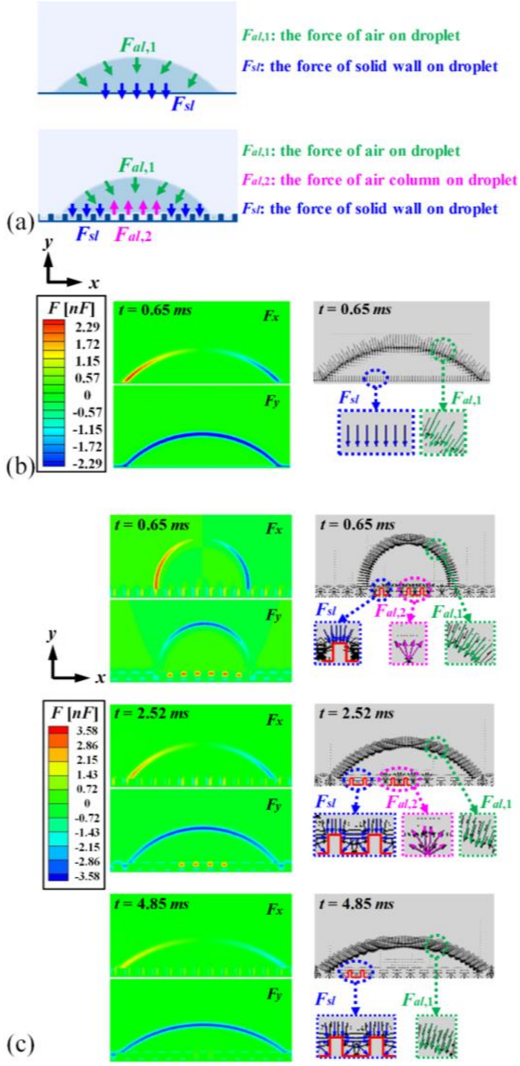

Fig. 8. (a) Analysis of the forces acting on the droplets on the smooth and micropillar surfaces. (b) The force contour and vector on the smooth surface at t = 0.65 *ms*. (c) The force contours and vectors on the micropillar surface at t = 0.65, 2.52, and 4.85 *ms*.

The normalized surface free energy is eventually calculated through substituting Eq. (19) into Eq. (18) to remove the unknown parameters of γ^{la}, γ^{as}, and γ^{sl}:

$$\frac{\Delta SE}{\gamma^{la}} = (A_{la} - A_{la0}) - A_{sl}\cos\theta_e \qquad (20)$$

where θ_e represents the static contact angle on a smooth surface.

The normalized surface free energy is calculated using Eq. (20), and the unit of $\Delta SE/\gamma^{la}$ is mm^2. For the sake of discussion, the surface free energy refers to the normalized surface free energy in the following sections. Figure 7(c) demonstrates a decreasing tendency of the surface free energy during the spreading process until the droplet reaches stability. As the droplet spreads out to a flat shape, the total surface free energy on all the interfaces minimizes as much as possible. The spreading process of the droplet takes a longer time on the micropillar surface than on the smooth surface. Moreover, regarding the micropillar surface, the surface free energy decreases considerably compared with the smooth surface. A smaller surface free energy indicates a smaller interfacial tension, resulting in a larger adhesion force of a solid surface. Hence, the surface free energy characteristics also support that the surface microstructure enhances the hydrophilicity.

To further discuss the mechanisms of droplet dynamics on smooth and micropillar surfaces, the forces acting on the droplets are analyzed. As given in Fig. 8(a), regarding the smooth surface, the forces affecting the wetting process mainly include the force of air on the droplet ($F_{al,1}$) and the force of the solid wall on the droplet (F_{sl}), both of which promote and accelerate the spreading process. Figure 8(b) demonstrates the force contour and vector on the smooth surface at t=0.65 *ms*. F_x and F_y represent the projective components of force along the *x* and *y* axes, respectively. In the contour of F_x, the forces exerted on the air-liquid interface ensure the stable spreading of the droplets, which is in accordance with that seen in nature. In the contour of F_y, the forces exerted on the air-liquid interface cause the droplets to tend to a flat shape. Meanwhile, the forces exerted on the solid–liquid interface serve as adhesion to promote the spreading process. In addition, the force vector is discussed, in which the forces can be divided into $F_{al,1}$ and F_{sl}, and are shown as partially enlarged drawings.

As given in Fig. 8(c) at t=0.65 *ms* and t=2.52 *ms*, regarding the micropillar surface, there are three kinds of forces influencing the droplet: the force of air on the droplet ($F_{al,1}$), the force of the air column on the droplet ($F_{al,2}$), and the force of the solid wall on the droplet (F_{sl}) before the liquid completely falls into the spaces between micropillars. In the contour of F_y, $F_{al,2}$ exists in the spaces between micropillars to hinder the droplet from adhering to the surface, serving as a resistance to the spreading process. Hence, $F_{al,2}$ is the crucial factor resulting in the stretching and hindering effect of the microstructure on the spreading process. However, the force vector demonstrates that $F_{al,1}$ and F_{sl} promote the spreading process, which act the same as those on the smooth surface. After the liquid completely fills in the spaces, there is no air between the droplet and micropillars. Therefore, at t=4.85 *ms*, the forces only include the force of air on the droplets ($F_{al,1}$) and the force of the solid wall on the droplets (F_{sl}). Both $F_{al,1}$ and F_{sl} contribute to the spreading process. Generally, the force discussions about the contours and vectors are in accordance with the analyses in Fig. 8(a).

3.3 Effect of the Micropillar Geometric Sizes on the Hydrophilicity

3.3.1 Single-factor Analysis of the Geometric Sizes

To explore the effect of the micropillar geometric sizes on the hydrophilicity, droplets spreading on micropillar surfaces were simulated by changing the pillar width a, height h, and pitch b. Here, the interaction strength $G_{ads,2}$ was set to 0.3, indicating a static contact angle θ_e of 44° on a smooth Ti surface. When varying only one pillar parameter of 1, 3, 5, 7, and 9 μm, the other two parameters remain unchanged at 5 μm.

As observed from Fig. 9, the contact angle and surface free energy initially increase and then decrease with an increasing pillar width a, increase with an increasing pillar height h, and decrease with an increasing pillar pitch d. In fact, Fig. 9 reflects the tendency of the surface hydrophilicity to change with a, h, and d.

As shown in Eq. (20), the surface free energy of a hydrophilic surface decreases with an increasing solid–liquid contact interface (A_{sl}), which indicates the enhancement of hydrophilicity. As shown in Fig. 10(a), A_{sl} consists of the horizontal contact area (blue region) and the side area of micropillars (yellow region); hence, A_{sl} is described as:

$$A_{sl} = \frac{\pi L^2}{4} + 4ahN \tag{21}$$

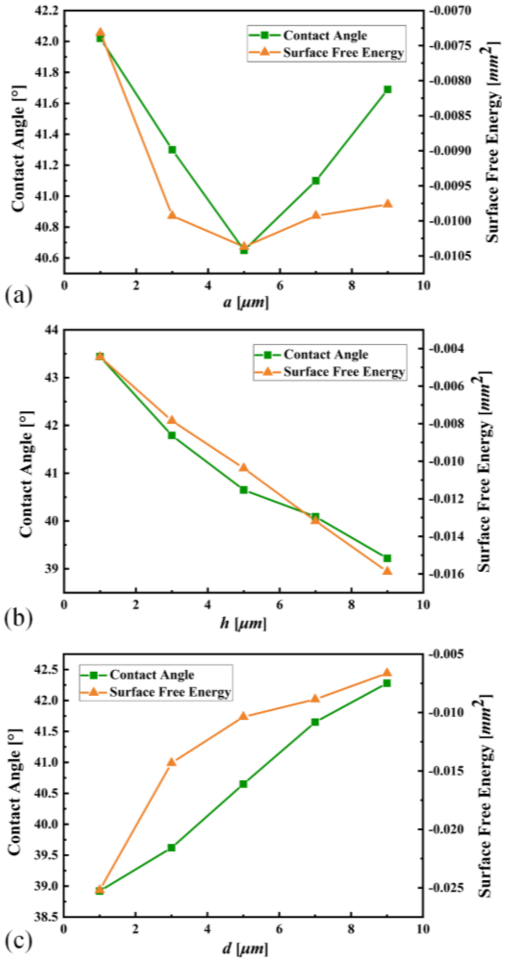

Fig. 9. Final contact angle and surface free energy of micropillar surfaces as a function of the pillar (a) width *a*, (b) height *h*, and (c) pitch *d*.

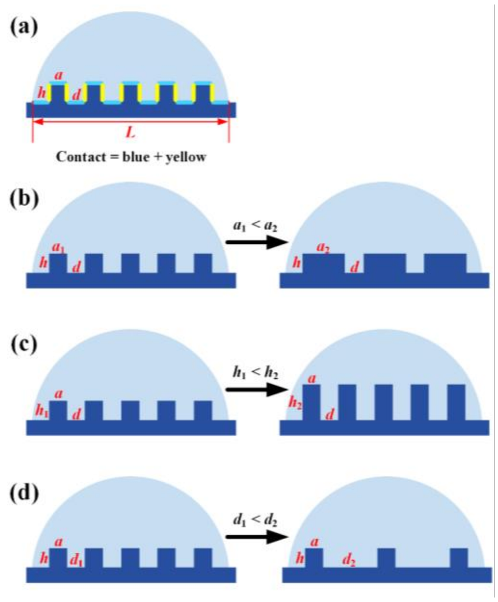

Fig. 10. (a) The contact interface of the liquid and solid on a micropillar surface. Comparison of the contact interfaces with different pillars: (b) width *a*, (c) height *h*, and (d) pitch *d*.

where N is the number of micropillars in the scope solid–liquid interface. N is given by:

$$N = \frac{\pi L^2}{4(a+d)^2} \tag{22}$$

Finally, A_{sl} can be calculated by substituting Eq. (22) into Eq. (21):

$$\begin{aligned} A_{sl} &= \frac{\pi L^2}{4} + \frac{\pi L^2 ah}{(a+d)^2} \\ &= \frac{\pi L^2}{4} + \frac{\pi L^2 h}{a + \frac{d^2}{a} + 2d} \end{aligned} \tag{23}$$

The contact line of a droplet is fixed as L. When changing the value of a, there is a maximum of A_{sl} at $a=d$ according to Eq. (23). Figure 10(c) shows that a larger value of h indicates a larger A_{sl}. In Fig. 10(d), the increase in d indicates a decrease in the number of micropillars, resulting in a decrease in A_{sl}. The result can also be obtained from Eq. (23). In conclusion, an appropriate a, a larger h, and a smaller d will lead to a larger A_{sl}, thus enhancing the hydrophilicity.

To validate the results, studies similar to our work are listed and compared. According to the work of Wang *et al*. (2020), an increase in the solid–liquid contact area indicates an increase in the liquid adhesion force and a decrease in the contact angle, which indicates a similar conclusion to Eq. (20). Zhang *et al*. (2012) considered the effect of tier structure parameters (height and pitch) on the surface free energy. Simulation results show that the surface free energy decreases with an increasing structure height and increases with an increasing structure pitch, which is consistent with the results presented in Figs. 9(b) and 9(c). In addition, Chen *et al.* (2022) experimentally explored the effect of the surface structure morphology on the hydrophilicity using a femtosecond pulsed laser method. With an increasing laser power, the etching depth of the surface structure increases, and the contact angle decreases, which is in accordance with the results presented in Fig. 9(b). With a decreasing scanning interval, the width of the surface structure increases, and the contact angle increases, which is partly consistent with the results presented in Fig. 9(a). Therefore, the results in this study are reliable. In addition, further and deeper investigation on the effect of the geometric sizes is necessary.

3.3.2 Response Surface Method Design

RSM is a widely used statistical analysis method that explores the effect of the experimental factors on the response variable, including the interaction between different factors (Guo *et al*. 2022). By fitting the functional relationship between the factors and the response variable, the optimal solution for the response variable is achieved.

Based on response surface theory, the Box–Behnken design (BBD) is a widely used experimental method (Pan *et al*. 2022). In this study, a pillar width a, a height h, and a pitch b are successively selected as the influence factors A, B, and C, and the contact angle value is set as the response variable. The levels of each factor are given in Table 1.

Table 1 Table of factor levels.

Parameters	Notation	Unit	Levels of Factors		
			-1	0	1
Pillar width (a)	A	μm	1	5	9
Pillar height (h)	B	μm	1	5	9
Pillar pitch (d)	C	μm	1	5	9

3.3.3 Response Surface Regression Model

The BBD experimental schemes and results are shown in Table 2. To analyze the functional relationship of the pillar parameters and the contact angle, the response surface regression model was established based on the results in Table 2 using Design-Expert. The quadratic polynomial regression equation shown in Eq. (24) can be utilized for predicting the response over the specified levels of each factor.

$$\begin{aligned} &\text{Contact Angle} = 40.6898 + 0.1928a - 1.3588h \\ &+1.1088d - 0.0106ah - 0.0681ad + 0.0466hd \\ &+0.0208a^2 + 0.0664h^2 - 0.0452d^2 \end{aligned} \tag{24}$$

Figure 11 shows the normal distribution of the residuals. The normal distribution of the residuals is approximately linear, which indicates the accuracy of the regression model.

Table 2 BBD experimental results.

Run	A: a [μm]	B: h [μm]	C: d [μm]	Contact Angle [°]
1	5	1	9	44.31
2	5	1	1	42.05
3	1	9	5	40.65
4	5	5	5	40.65
5	1	5	1	36.23
6	9	5	1	39.25
7	9	9	5	39.58
8	9	5	9	42.11
9	9	1	5	43.78
10	1	5	9	43.45
11	1	1	5	44.17
12	5	9	9	41.42
13	5	5	5	40.65
14	5	9	1	36.18
15	5	5	5	40.65
16	5	5	5	40.65
17	5	5	5	40.65

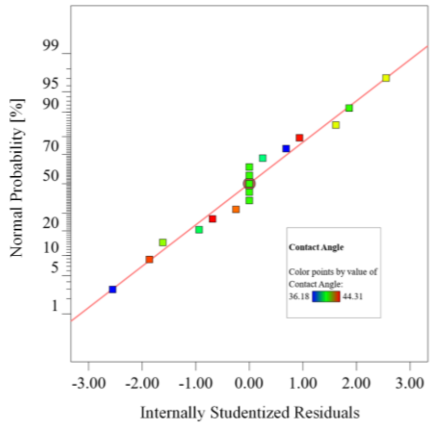

Fig. 11. Normal distribution of the residuals.

3.3.4 Response Surface Analysis

To verify the accuracy of Eq. (24), Table 3 displays the variance analysis about the regression model. The F value of the model is 30.7, and the p value is lower than 0.0001, which indicates that the regression model is very significant. In addition, the correlation coefficient for determining the model R^2=0.9754 reflects the high accuracy of the regression model.

The p values of the pillar height h (B) and pitch d (C) are less than 0.0001, reflecting the highly significant effects of h and d on the contact angle. However, the p value of the pillar width a (A) is greater than 0.05, which indicates that the effect of a on the contact angle is not significant. The values of the mean square suggest the level of influence factors: C > B > A. Among the interaction terms, the AC and BC interaction effects are significant.

To further investigate the interaction effect of different factors on the contact angle, 3D response surfaces and corresponding contour diagrams are given in Fig. 12. Figure 12(a) displays the interaction between the pillar width a (A) and height h (B) with the pillar pitch d (C) fixed at the intermediate level. The contact angle decreases with an increasing pillar height. In addition, with an increasing pillar width, the contact angle initially decreases and then increases. The contour distribution demonstrates that a smaller contact angle is available when the pillar height is 5-9 μm and the pillar width is 2-9 μm.

Figure 12(b) shows the interaction between the pillar width a (A) and pitch d (C) with the pillar height h (B) fixed at the intermediate level. Analysis of the 3D response surface reflects that the contact angle increases with an increasing pillar pitch. The increasing tendency is more obvious if the pillar width is small. However, the relationship between the pillar width and contact angle depends on the value of the pillar pitch. The contact angle increases with an increasing pillar width when the pillar pitch is small and decreases with an increasing pillar width when the pillar pitch is large. The contour distribution demonstrates that a smaller contact angle is available when the pillar pitch is 1-2 μm and the pillar width is 1-3 μm. Figure 12(c) shows the interaction between the pillar height h (B) and pitch d (C) with the pillar width a (A) fixed at the intermediate level. The contact angle increases with an increasing pillar pitch. In addition, the contact angle decreases with an increasing pillar height. The contour distribution demonstrates that a smaller contact angle is available when the pillar pitch is 1-3 μm and the pillar height is 5-9 μm.

3.3.5 Optimization and Validation

To achieve the optimal hydrophilicity of the micropillar surface, the minimum contact angle and corresponding combination of factors are obtained through the response surface optimization methodology. According to the results from Design-Expert, the minimum value of the contact angle is 35.373° when the pillar width is 1 μm, the height is 9 μm, and the pitch is 1 μm.

Table 3 Variance analysis of the regression model.

Source	Sum of Squares	Df	Mean Square	F value	p value	
Model	86.83	9	9.65	30.7	< 0.0001	*significant*
A-a	0.0061	1	0.0061	0.0193	0.8936	
B-h	33.95	1	33.95	108.03	< 0.0001	
C-d	38.63	1	38.63	122.94	< 0.0001	
AB	0.1156	1	0.1156	0.3679	0.5633	
AC	4.75	1	4.75	15.12	0.006	
BC	2.22	1	2.22	7.06	0.0326	
A^2	0.4655	1	0.4655	1.48	0.263	
B^2	4.75	1	4.75	15.13	0.006	
C^2	2.2	1	2.2	6.99	0.0332	
Residual	2.2	7	0.3142			
Lack of Fit	2.2	3	0.7332			
Pure Error	0	4	0			
Cor Total	89.03	16				
R^2 = 0.9754				R^2_{adj} = 0.9436		

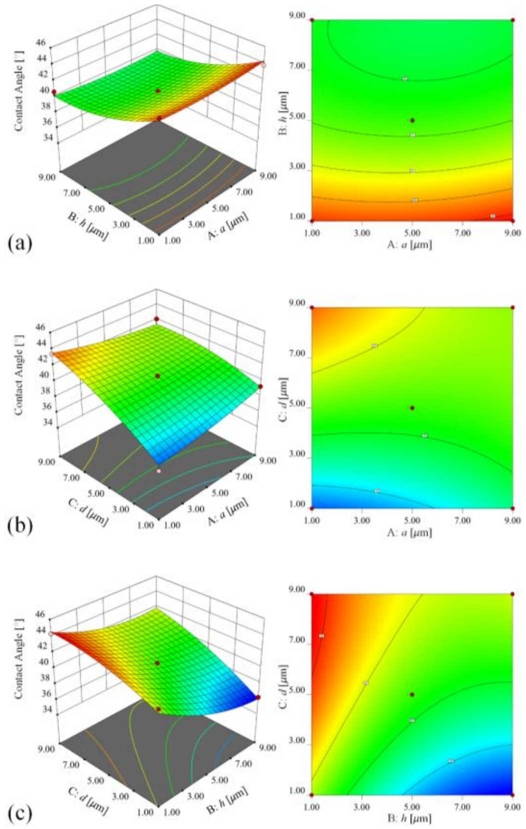

Fig. 12. Response surface and contour diagrams for the analyses of the (a) AB interaction term, (b) AC interaction term, and (c) BC interaction term.

The accuracy of the optimization prediction was verified, and the results are given in Table 4. By comparing the simulation result with the predicted value, the regression model is considered to be accurate and reliable with an error of 0.687%.

Table 4 Comparison of the simulation result and response surface optimization value.

a [μm]	h [μm]	d [μm]	LBM result [°]	Predicted value [°]	Error [%]
1	9	1	35.13	35.373	0.687

3.4 Effect of the Surface Roughness and Geometric Shape on the Hydrophilicity

Here, a normalized surface area or dimensionless parameter of the micropillar is defined to integrate the geometric parameters and denote the surface roughness (Aldhaleai and Tsai 2020). The roughness parameter ξ is defined as:

$$\xi = 1 + \frac{4ah}{(a+d)^2} \tag{25}$$

According to Eq. (25), ξ of a smooth surface equals 1, and ξ of a micropillar surface is more than 1.

For the cases already simulated in Section 3.3, the surface roughness parameters were calculated, and the results of all the cases were added for discussion. In addition, the supplementary cases listed in Table 5 were also simulated to investigate the effect of the surface roughness.

Table 5 Supplementary cases for discussion.

Cases	a [μm]	h [μm]	d [μm]	ξ
1	3	10	3	4.333
2	5	10	2	5.082
3	5	10	1	6.556
4	5	15	2	7.122
5	2	15	2	8.500
6	5	15	1	9.333

Figure 13 demonstrates the final contact angle and surface free energy of micropillar surfaces as a function of the surface roughness ξ. As ξ increases, the contact angle decreases, indicating a gradually enhancing hydrophilicity. In addition, the decreasing surface free energy indicates a decreasing tendency of the interfacial tension, which results in a larger adhesion force of the surface. In summary, for an intrinsic hydrophilic Ti surface, the micropillar will enhance the hydrophilicity. Moreover, the increase in the surface roughness indicates an increase in the solid–liquid contact interface (A_{sl}). As shown by Eq. (20), the surface free energy of a hydrophilic surface decreases with A_{sl}, which suggests an increase in the hydrophilicity. Therefore, the increase in the surface roughness results in the enhancement of the hydrophilicity.

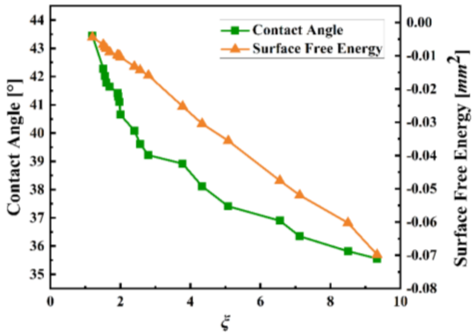

Fig. 13. Final contact angle and surface free energy of micro-structured surfaces as a function of the surface roughness parameter ξ.

To examine the effect of the geometric shape on the hydrophilicity, droplet dynamics on the surfaces with hemispheric or zig-zag microstructures were simulated and analyzed. Figure 14 shows the geometric parameters of the hemispheric and zig-zag microstructures. Referring to the definition of the surface roughness on a micropillar surface, the roughness parameter ξ of the surface with hemispheric microstructure is defined as:

$$\xi = 1 + \frac{\pi R^2}{(2R+d)^2} \tag{26}$$

Similarly, the roughness parameter ξ of the surface with a zig-zag microstructure is described as:

$$\xi = 1 + \frac{\pi R(\sqrt{R^2+h^2} - R)}{(2R+d)^2} \tag{27}$$

The parameter design is given in Table 6. The effect of the geometric shape was discussed and analyzed by designing the same value of the roughness parameter for different geometric shapes. In addition, by changing the value of ξ, the effect of the roughness parameter on the hydrophilicity was again verified.

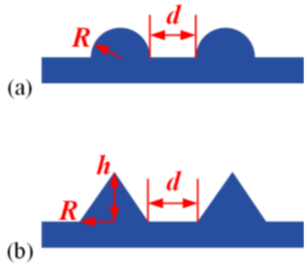

Fig. 14. (a) Surface with a hemispheric microstructure showing the radius *R* and pitch *d*. (b) Surface with a zig-zag microstructure showing the radius *R*, height *h*, and pitch *d*.

Table 6 Parameter design for the discussion of the geometric shape.

Pillar Microstructure	a [μm]	3	3	7
	h [μm]	3	3	4
	d [μm]	16	7	5
Hemispheric Microstructure	R [μm]	4	5	5
	d [μm]	15	5	0
Zig-zag Microstructure	R [μm]	4	4	3
	h [μm]	7	7	11
	d [μm]	15	4	4
ξ		1.09	1.35	1.78

Figure 15(a) shows the effect of the different geometric shapes on the final contact angle. Among the three different geometric shapes, the contact angle of the surface with the pillar microstructure is smallest when ξ remains the same. Therefore, the pillar microstructure demonstrates the best hydrophilicity with little difference between the hemispheric and zig-zag microstructures.

The wetting pattern is the Cassie state when the droplet contacts the microstructure at the beginning. Figure 15(b) shows the solid–liquid interface (red region) of different microstructure shapes in the Cassie state. The contact area of the pillar microstructure is largest, thus generating the largest adhesion force to drive the spreading motion of the droplet. Therefore, the surface with a pillar microstructure demonstrates the best hydrophilicity, as shown in Fig. 15(c).

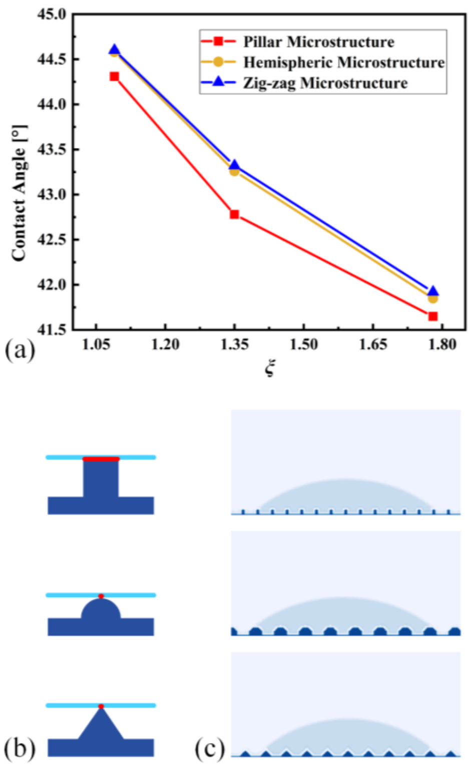

Fig. 15. (a) Final contact angle as a function of the roughness parameter on different microstructure surfaces. (b) The solid–liquid contact interface in the Cassie state. (c) Images of droplets at the final time for the same value of surface roughness.

4. CONCLUSION

In this study, an LB model was proposed for analyzing droplet dynamics on Ti surfaces with specific microstructures and roughness designs. Here, the SC multi-component multi-phase model was applied in the simulations. We simulated droplet spreading on smooth and micropillar surfaces with various wettability. The results show that the micropillar (a=5 μm, h=5 μm, and d=5 μm) used in our simulations enhances the hydrophobicity when $G_{ads,2}$ is less than 0.1 and enhances the hydrophilicity when $G_{ads,2}$ is more than 0.2. To reveal more details and mechanisms, a comparison of droplet dynamics on hydrophilic smooth and micropillar surfaces was conducted in terms of the edge locations, contact line, droplet height, contact area, surface free energy, and forces. Compared with the smooth surface, the micropillar (a=5 μm, h=5 μm, and d=5 μm) obviously stretches and impedes the spreading process due to the air in the spaces between micropillars, which can be supported by the force analyses. In addition, the normalized surface free energy also demonstrates that the micropillar surface provides a smaller interfacial tension, leading to a stronger adhesion force and better hydrophilicity. Afterward, we investigated the effects of the micropillar geometric sizes on the hydrophilicity via single factor analysis and RSM. These methods show that hydrophilicity initially increases and then decreases with an increasing a, increases with an increasing h, and decreases with an increasing d. In addition, the interaction effects of a-d and h-d are significant. The optimization validation of the RSM also demonstrates the accuracy of our LB model, which has an error of only 0.687%. Finally, a dimensionless parameter of the micropillar was defined to integrate the geometric parameters and denote the surface roughness. The results suggest that the hydrophilicity of Ti surfaces improves with an increasing surface roughness. In addition, the effect of the microstructure shape was investigated using the same value for the surface roughness. Compared with the hemispheric and zig-zag microstructures, surfaces with micropillars demonstrate the best hydrophilicity. The proposed LB model is useful and reliable for analyzing and predicting droplet dynamics on micro-structured Ti surfaces. It is expected to provide an instrumental tool for improving the intrinsic hydrophilicity of Ti surfaces via microstructure and roughness design.

ACKNOWLEDGEMENTS

The authors would like to acknowledge the financial support by the National Natural Science Foundation of China (Grant Nos. 51625601) and the Science Foundation of Union Hospital (No. 2021xhyn090).

REFERENCES

Abhijith, N. V., C. P. Priyanka, U. Sudeep and K. K. Ramachandran (2021). Crystallinity and wettability induced osteogenic behaviors of commercially pure Ti and Ti-6Al-4V alloy implant surfaces having multiscale surface topography. *Materials Today: Proceedings* 46(19), 9405-9411.

Aldhaleai, A. and P. A. Tsai (2020). Effect of a cationic surfactant on droplet wetting on superhydrophobic surfaces. *Langmuir* 36(16), 4308-4316.

Cassie, A. B. D. and S. Baxter (1944). Wettability of porous surfaces. *Transactions of the Faraday Society* 40, 546-551.

Chen, Y., W. P. Peng, X. F. Hu and C. Zhang (2022). Functional performance of Silicon with periodic surface structures induced by femtosecond pulsed laser. *Coatings* 12(6), 716.

Davar, H., N. M. Nouri and M. Navidbakhsh (2021). Effects of superhydrophobic, hydrophobic and hybrid surfaces in condensation heat transfer. *Journal of Applied Fluid Mechanics* 14(4), 1077-1090.

Díaz-Cuenca, A., D. Rabadjieva, K. Sezanova, R. Gergulova, R. Ilieva and S. Tepavitcharova (2022). Biocompatible calcium phosphate-based ceramics and composites. *Materials Today: Proceedings* 61(4), 1217-1225.

Dong, Y. Q., L. Long, P. Zhang, D. P. Yu, Y. N. Wen, Z. Zheng, J. Wu and W. Chen (2021). A chair-side plasma treatment system for rapidly enhancing the surface hydrophilicity of titanium dental implants in clinical operations. *Journal of Oral Science* 63(4), 334-340.

Du, P., D. Song, F. Ren, Q. Xue and H. Hu (2017). Flow characterizations and drag reduction on the hydrophobic surface with a full covering gas film. *Journal of Applied Fluid Mechanics* 10(2), 491-498.

Ezzatneshan, E. (2019). Simulation of dipole vorticity dynamics colliding viscous boundary layer at high Reynolds numbers. *Journal of Applied Fluid Mechanics* 12(4) 1073-1081.

Ezzatneshan, E. and H. Vaseghnia (2019). Evaluation of equations of state in multiphase lattice Boltzmann method with considering surface wettability effects. *Physica A: Statistical Mechanics and its Applications* 541, 123258.

Ezzatneshan, E. and R. Goharimehr (2021). A pseudopotential lattice boltzmann method for simulation of two-phase flow transport in porous medium at high-density and high–viscosity ratios. *Geofluids* 2021, 5668743.

Fei, L. L., F. F. Qin, G. Wang, K. H. Luo, D. Derome and J. Carmeliet (2022). Droplet evaporation in finite-size systems: Theoretical analysis and mesoscopic modeling. *Physical Review E* 105(2), 025101.

Guo, L. X., Y. H. Guo, L. Zhong and J. T. Zhu (2022). Research on back analysis of meso-parameters of hydraulic cemented sand and gravel based on Box-Behnken design response surface. *Science and Engineering of Composite Materials* 29(1), 84-96.

He, W., P. Yao, D. Chu, H. Sun, Q. Lai, Q. Wang, P. Wang, S. Qu and C. Huang (2022). Controllable hydrophilic titanium surface with micro-protrusion or micro-groove processed by femtosecond laser direct writing. *Optics & Laser Technology* 152, 108082.

Huang, H., D. T. Thorne, M. G. Schaap and M. C. Sukop (2007). Proposed approximation for contact angles in Shan-and-Chen-type multicomponent multiphase lattice Boltzmann models. *Physical Review E* 76, 066701.

Li, M., S. Komasa, S. Hontsu, Y. Hashimoto and J. Okazaki (2022). Structural characterization and osseointegrative properties of pulsed laser-deposited fluorinated hydroxyapatite films on nano-Zirconia for implant applications. International *Journal of Molecular Sciences* 23(5), 2416.

Liddell, R. S., Z. M. Liu, V. C. Mendes and J. E.

Davies (2020). Relative contributions of implant hydrophilicity and nanotopography to implant anchorage in bone at Early Time Points. *Clinical Oral Implants Research* 31(1), 49-63.

Lin, G., C. Geng, L. Zhang and F. Hut (2022). Improved multicomponent multiphase lattice Boltzmann model for physical foaming simulation. *Journal of Applied Fluid Mechanics* 15(4), 1125-1136.

Mohammadrezaei, S., M. Siavashi and S. Asiaei (2022). Surface topography effects on dynamic behavior of water droplet over a micro-structured surface using an improved-VOF based lattice Boltzmann method. *Journal of Molecular Liquids* 350, 118509.

Mosas, K. K. A., A. R. Chandrasekar, A. Dasan, A. Pakseresht and D. Galusek (2022). Recent advancements in materials and coatings for biomedical implants. *Gels* 8(5), 323.

Pan, C. F., Z. Chen, Q. M. Tang, Z. G. He, L. M. Wang, H. H. Li and W. Q. Zhou (2022). Heat dissipation improvement of Lithium battery pack with liquid cooling system based on Response-Surface optimization. *Journal of Energy Engineering* 148(4), 1943-7897.

Panda, D., S. Bhaskaran, S. Paliwal, A. Kharaghani, E. Tsotsas and V. K. Surasani (2020). Pore-scale physics of drying porous media revealed by Lattice Boltzmann simulations. *Drying Technology* 40(6), 1114-1129.

Park, J. W., J. H. Seo and H. J. Lee (2022). Enhanced osteogenic differentiation of mesenchymal stem cells by surface lithium modification in a sandblasted/acid-etched titanium implant. *Journal of Biomaterial Applications* 37(3), 447-458.

Pham, D. Q., S. Gangadoo, C. C. Berndt, J. Chapman, J. L. Zhai, K. Vasilev, V. K. Truong and A. S. Ang (2022). Antibacterial longevity of a novel Gallium liquid metal/hydroxyapatite composite coating fabricated by plasma spray. *ACS Applied Materials & Interfaces* 14(16), 18974-18988.

Sun, Y. L., A. Rahmani, T. Saeed, M. Zarringhalam, M. Ibrahim and D. Toghraie (2021). Simulation of deformation and decomposition of droplets exposed to electro-hydrodynamic flow in a porous media by lattice Boltzmann method. *Alexandria Engineering Journal* 61(1), 631-646.

Tallet, L., V. Gribova, L. Ploux, N. E. Vrana and P. Lavalle (2021). New smart antimicrobial hydrogels, nanomaterials, and coatings: earlier action, more specific, better dosing? *Advanced Healthcare Materials* 10(1), 2001199.

Tao, B. L., W. K. Zhao, C. C. Lin, Z. Yuan, Y. He, L. Lu, M. Chen, Y. Ding, Y. Yang, Z. Xia and K. Cai (2020). Surface modification of titanium implants by ZIF-8@Levo/LBL coating for inhibition of bacterial-associated infection and enhancement of in vivo osseointegration. *Chemical Engineering Journal* 390, 124621.

Wang, D. H., Q. Q. Sun, M. J. Hokkanen, C. L. Zhang, F. Y. Lin, Q. Liu. S. P. Zhu, T. Zhou, Q. Chang, B. He and Q. Zhou (2020). Design of robust superhydrophobic surfaces. *Nature* 582(7810), 55-59.

Wang, H., J. Q. Liu, C. T. Wang, S. G. Shen, X. D. Wang and K. L. Lin (2021). The synergistic effect of 3D-printed microscale roughness surface and nanoscale feature on enhancing osteogenic differentiation and rapid osseointegration. *Journal of Materials Science & Technology* 63, 18-26.

Wang, M. H., Y. M. Xiong, L. M. Liu and G. Peng (2018). LBM investigation of immiscible displacement in a channel with regular surface roughness. *Transport in Porous Media* 123(1), 195-215.

Wang, X., B. Xu, Y. Wang and Z. Q. Chen (2019). Directional migration of single droplet on multi-wetting gradient surface by 3D lattice Boltzmann method. *Computers & Fluids* 198, 104392.

Wenzel, R. N. (1936). Resistance of solid surfaces to wetting by water. *Transactions of The Faraday Society* 28(8), 988-994.

Yan, X. X., W. Cao and H. H. Li (2022). Biomedical alloys and physical surface modifications: A Mini-Review. *Materials* 15(1), 66.

Yang, W. E. and H. H. Huang (2021). TiO2 nanonetwork on rough Ti enhanced osteogenesis in vitro and in vivo. *Journal of Dental Research* 100(10), 1186-1193.

Yin, Q., Q. Guo, Z. L. Wang, Y. Q. Chen, H. G. Duan and P. Cheng (2021). 3D-Printed bioinspired Cassie-Baxter wettability for controllable microdroplet manipulation. *ACS Applied Materials & Interfaces* 13(1), 1979-1987.

Zhang, B. J., J. Park, K. J. Kim and H. Yoon (2012). Biologically inspired tunable hydrophilic/hydrophobic surfaces: a copper oxide self-assembly multitier approach. *Bioinspiration & Biomimetics* 7(3), 036011.

Zhang, X. Y., M. Y. Huang, Q. Ji and X. B. Luo (2018). Lattice Boltzmann modeling and experimental study of water droplet spreading on wedge-shaped pattern surface. *International Journal of Heat and Mass Transfer* 130, 857-861.

Zhang, Z. C., R. G. Xu, Y. Yang, C. A. Liang, X. L. Yu, Y. Liu, T. Wang, Y. Yu and F. Deng (2021). Micro/nano-textured hierarchical titanium topography promotes exosome biogenesis and secretion to improve osseointegration. *Journal of Nanobiotechnology* 19(1), 78.